Stimulated Raman scattering from Mie-resonant subwavelength nanoparticles

George P. Zograf,[†] Daniil Ryabov,[†] Viktoria Rutckaia,[‡] Pavel Voroshilov,[†] Pavel Tonkaev,[†] Dmitry V. Permyakov,[†] Yuri Kivshar,[*,†,¶] and Sergey V. Makarov[*,†]

[†]*Department of Physics and Engineering, ITMO University, St. Petersburg 197101, Russia*

[‡]*Center for Innovation Competence SiLi-Nano, Martin-Luther-University Halle-Wittenberg, 06120 Halle (Saale), Germany*

[¶]*Nonlinear Physics Centre, Australian National University, Canberra ACT 2601, Australia*

E-mail: yuri.kivshar@anu.edu.au; s.makarov@metalab.ifmo.ru

Abstract

Resonant dielectric structures have emerged recently as a new platform for subwavelength non-plasmonic photonics. It was suggested and demonstrated that magnetic and electric Mie resonances can enhance substantially many effects at the nanoscale including spontaneous Raman scattering. Here we demonstrate *stimulated Raman scattering* (SRS) for isolated crystalline silicon (c-Si) nanoparticles and observe experimentally a transition from spontaneous to stimulated scattering manifested in a nonlinear growth of the signal intensity above a certain pump threshold. At the Mie resonance, the light gets confined into a low volume of the resonant mode with enhanced electromagnetic fields inside the c-Si nanoparticle due to its high refractive index, which leads to an overall strong SRS signal at low pump intensities. Our finding paves the way to the development of efficient Raman nanolasers for multifunctional photonic metadevices.

KEYWORDS: Stimulated Raman scattering, Mie resonances, crystalline silicon, nanoparticles, nonlinear nanophotonics, multipolar mode expansion.

Raman scattering is a powerful tool for analyzing both plasmonic[1,2] and dielectric[3–5] optical structures. Semiconductors, which are often considered as relevant materials for all-dielectric photonics, have a strong inherent Raman response due to their crystalline lattice structure. In particular, crystalline silicon (c-Si) has a sharp Raman line around 520 cm^{-1}, caused by the interaction of light with optical phonons. A few years ago, it was demonstrated experimentally[6] that this Raman response can be enhanced resonantly through the excitation of magnetic dipole Mie modes in dielectric nanostructures.

Spontaneous Raman scattering enhanced by the electric and magnetic Mie resonances of subwavelength particles[6,7] was suggested for sensing[5], nanothermometry[8,9], and controllable drug delivery[10]. However, spontaneous Raman scattering remains a relatively weak effect as compared with luminescence observed in resonant dielectric nanostructures[11–13]. A transition from spontaneous to stimulated Raman emission[14] empowered by Mie resonances is expected to enhance the scattering efficiency in subwavelength photonics.

The high-quality-factor (high-Q factor) Raman microlasers were first demonstrated for micrometer-size liquid droplets[15,16] and silica microspheres[17]. To shrink the resonator dimensions, one needs employing semiconductors, and the Raman gain about 10^5 times higher than that for silica has been demonstrated for silicon resonators[18–20]. Stimulated Raman scattering (SRS) was achieved in cavity-enhanced nanowires longer than 1 μm[21,22], with the pump intensities larger than 10 kW/cm^2, being accompanied by strong overheating.

In this Letter, we observe experimentally, for the first time to our knowledge, SRS from isolated subwavelength c-Si nanoparticles empowered by multipolar Mie resonances. We optimize the parameters of both nanoparticles and a substrate to achieve enhanced stimulated emission without overheating. This approach provides an additional degree of freedom for achieving the highest Raman scattering yield from fully subwavelength all-dielectric nanoscale structures, and it may be employed for useful functionalities such as sensing and

nanothermometry.

Results

Sample fabrication and characterization. Our samples are made from a silicon-on-sapphire wafer with a thickness of the c-Si film of 600 nm. The nanoparticles have the shape of nanodisks [or nanopillars, see Fig. 1(a)] with diameters 200÷1000 nm, and they are fabricated by electron-beam lithography (for details, see Methods below). Distance between isolated nanoparticles is 50 μm (all additional details are given in Supporting Information) and this removes any effect of neighboring particles in confocal optical measurements. Figures 1(b,c) show the SEM images of typical nanoparticles used in the experiment.

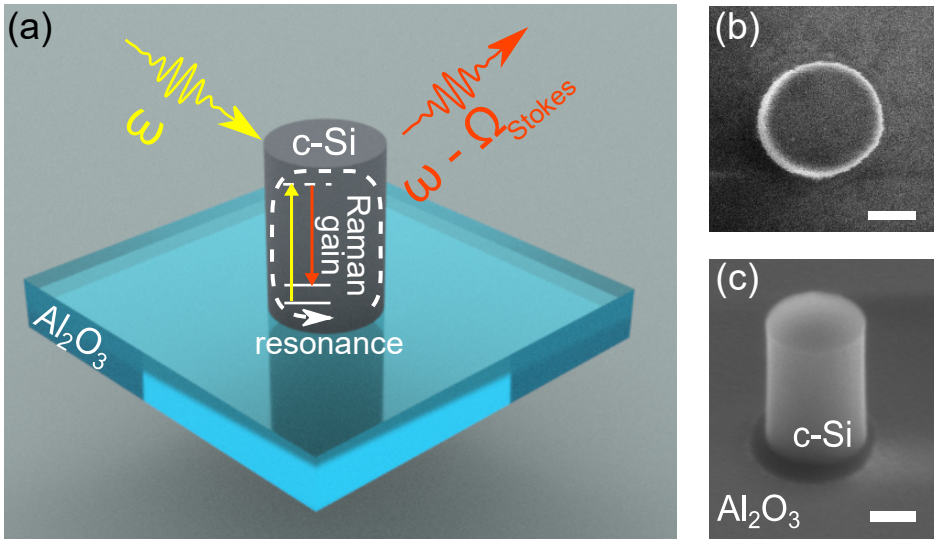

Figure 1: **Mie-resonant c-Si nanoparticle on a substrate for SRS experiments.** (a) Schematic view of a Si nanoparticle excited with a laser light. (b,c) Top and side SEM images of a c-Si nanoparticle fabricated on a sapphire substrate. Scale bars are 200 nm.

Optical Mie-type resonances in nanoparticles can be characterized experimentally by dark-field spectroscopy, when white light is illuminated on an isolated nanoparticle under an oblique incidence, and the scattered signal is collected by an objective, being then sent to a spectrometer and CCD camera (for details, see Methods below; the optical setup is shown in Supporting Information). Experimental dark-field spectra are shown in Fig. 2(a),

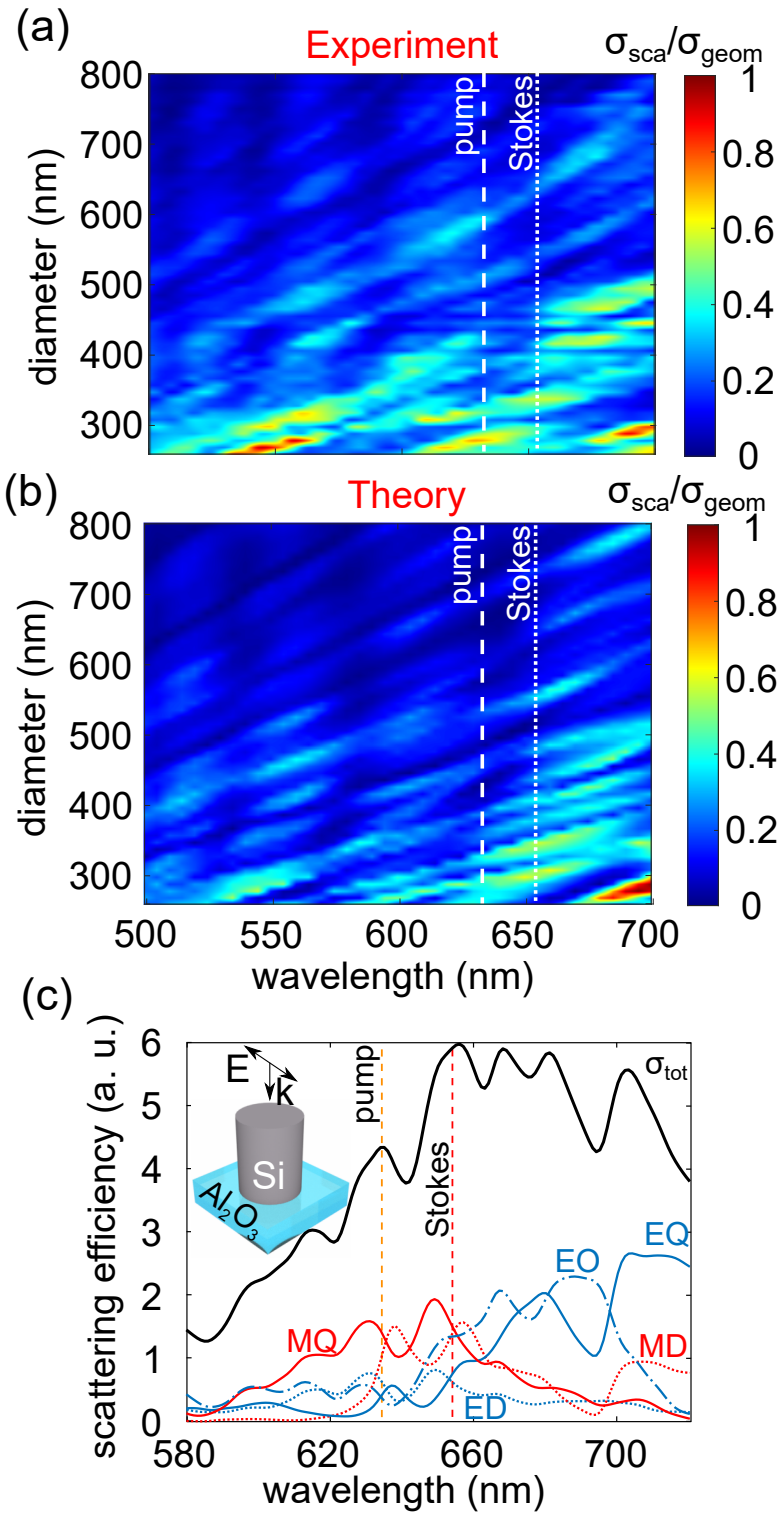

Figure 2: **White-light scattering by Si nanoparticles.** (a) Experimental and (b) theoretical dark-field white-light scattering (spectral range 500÷700 nm) from the Si nanoparticles with diameters 250÷800 nm and height 600 nm. (c) Theoretical dark-field spectrum analyzed with the modal decomposition for the 475-nm nanoparticle, corresponding to the SRS experiment. Here ED, MD, MQ, EQ and EO are electric dipole, magnetic dipole, magnetic quadrupole, electric quadrupole, and electric octupole, respectively.

and they should be compared with numerically simulated white-light scattering spectra of Fig. 2(b) (see Methods below for details of calculations). These results reveal the excitation of Mie resonances, that can be characterized by applying the multipole mode decomposition, as shown in Fig. 2(c) (see also Supporting Information).

As is known, *spontaneous* Raman scattering was demonstrated to be a very useful tool in the study of optical modes, because it involves the emission from a bulk of nanoparticles[6,8,23]. Strongly enhanced Raman scattering signal corresponds to an efficient energy coupling to the nanoparticle modes. In order to select the subwavelength nanoparticle with the strongest Raman scattering signal, we carry out the confocal Raman scattering measurements from individual c-Si nanoparticles (for details, see Methods), and obtain the size dependence of the signal excited at a pump wavelength of 633 nm, as summarized in Fig. 3(a). The beam radius of focused light is estimated to be around $r \approx 0.5\ \mu m$. Remarkably, the sapphire substrate with thermal conductivity almost 50 times higher than that of glass provides an excellent thermal sink for the nanoparticles possessing a good thermal contact with a substrate. That is why we do not observe in experiment any overheating effects in the Raman scattering signal with an additional shift and broadening, as was reported previously for nanospheres[8] and nanowires[22] placed on a glass substrate. In our experiments at low intensity (less than 0.1 mW/μm^2), the maximum Raman scattering signal corresponds to the nanoparticle diameter of 475 nm, being driven mostly by the MQ (third order) and MD (third order) modes, both at 654 nm and 633 nm wavelengths, as confirmed by the multipole mode decomposition in Fig. 2(c).

Stimulated Raman amplification. Figure 3(b) shows typical experimental dependencies of Raman scattering signal vs. pump intensity. At low intensities, spontaneous Raman scattering dominates being characterized by a linear dependence on the incident power, as was demonstrated earlier with c-Si nanoparticles[6,8]. However, at higher intensities (higher than 0.3 MW/cm^2), we observe a nonlinear growth of the Raman scattering signal for the nanodisk with diameter 475 nm, which is not observed for other nanodisks

with diameters 250÷800 nm, see a dashed line with blue squares in Fig. 3(b). This sharp difference characterizes the SRS regime. The Raman spectra are shown in Fig. 3(c) for a c-Si nanoparticle with diameter 475 nm and height 600 nm.

In the SRS regime, a stronger pump transfers a part of its energy to a weaker red-shifted Raman signal (i.e. at the Stokes wavelength or frequency) by interacting with a nonlinear medium. As a result, a weak Stokes beam can be amplified by the pump, and this process is attributed to the Raman amplification. The Raman amplification is the third-order nonlinear process described with nonlinear susceptibility, $\chi^{(3)}_{NR}(\omega_S;\omega_P,-\omega_P,\omega_S)$, or simpler $\chi^{(3)}_{NR}(\omega_S)$. The amplification can be characterized by the Raman gain of the Stokes wave,

$$g = -\frac{3\omega_S}{n_S n_P c^2 \varepsilon_0}\mathrm{Im}[\chi^{(3)}_{\mathrm{NR}}(\omega_{\mathrm{S}})], \tag{1}$$

where ω_S is the frequency of the Stokes photons, n_S (or n_P) is the refractive index at the Stokes (or pump) frequency, c is the speed of light, and ε_0 is permittivity of vacuum. For Si at near infrared frequencies, a typical gain is $g \approx 80$ cm/GW [18,24], and it depends on crystalline properties of c-Si and the pump wavelength. For example, the Raman gain depends linearly on the Stokes frequency[24], and its value can be several times larger than in the visible frequency range where, however, optical losses are often higher.

When the pump photons become trapped by a resonator mode, the Raman scattering gets enhanced, and it should generate a signal that grows exponentially with the input intensity (I_P), being characterized by the gain factor[25]:

$$I^{\mathrm{NR}}_{\mathrm{S}} \sim \exp(gI_P L_S), \tag{2}$$

where $I^{\mathrm{NR}}_{\mathrm{S}}$ is the intensity of the nonlinearly amplified Raman scattering signal at the Stokes frequency (ω_S), and the effective interaction length L_S is described as: $L_S = Q_S\lambda_S/2\pi n$. Experimentally measured data for the nonlinear Raman scattering signal can be fitted with this exponential dependence vs. incident intensity, where the transition from spontaneous scat-

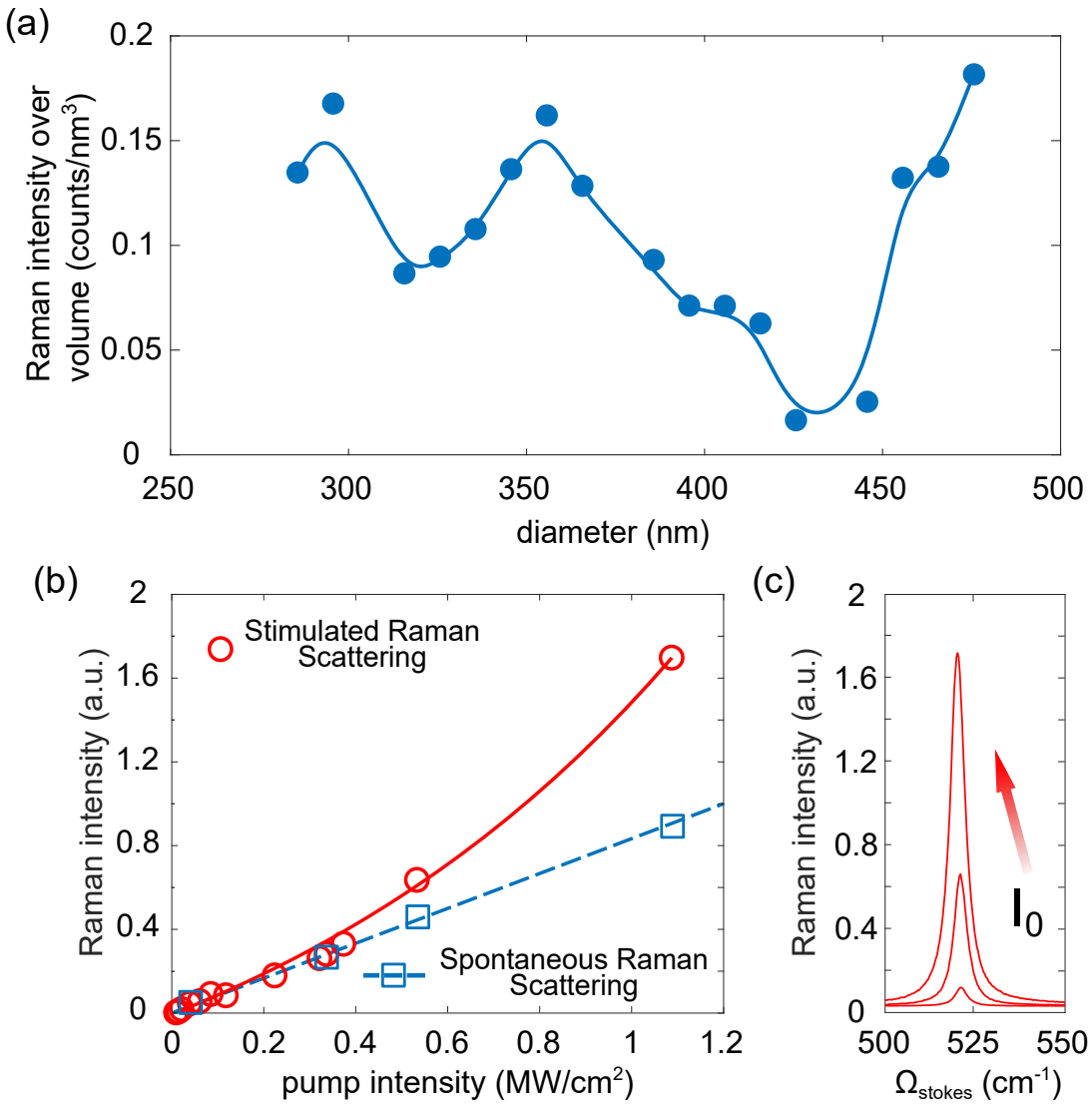

Figure 3: **Experimental Raman scattering from c-Si nanoparticles.** (a) Raman scattering intensity for varying diameters of nanoparticles measured at 0.22 MW/cm^2 intensity at pump wavelength 633 nm. (b) Experimental Raman scattering intensities at different pumps for the resonant 475-nm nanoparticle (red circles) and nonresonant 445-nm nanoparticle (blue squares). The red line corresponds to an exponential fitting based on Eq. (2). (c) SRS spectra for the 475-nm nanoparticle at the pump intensities: 0.1, 0.55, and 1.1 MW/cm^2. An arrow shows a growth of the pump intensity.

tering to the SRS amplification occurs at $I_{\mathrm{P}}^{\mathrm{tr}} \approx 0.4$ MW/cm^2, and this dependence deviates from a linear regime thus characterizing the SRS process.

Further, the Raman lasing threshold can be achieved when the resonator round-trip gain becomes equal to its round-trip loss. Generally, the threshold power can be estimated from the equation[17,26]:

$$P_{\mathrm{th}} \approx \frac{n_S n_P}{\lambda_S \lambda_P} \frac{V_{\mathrm{eff}}}{Q_S Q_P} \frac{\pi^2}{g} \frac{1}{B\Gamma} \tag{3}$$

where P_{th} is the incident pump power that differs from the power coupled to the resonator, n_P (or n_S) is the index of refraction at the pump (or Stokes) wavelength, V_{eff} is the effective mode volume at Stokes wavelength, λ_p and λ_S are the pump and Stokes wavelengths, respectively, g is the nonlinear bulk Raman gain coefficient, Q_P (or Q_S) is the total Q factor for the resonant mode excited at the pump (or Stokes) wavelength, B is the coupling efficiency, and Γ is the spatial overlap factor of the modes.

Remarkably, for luminescence and lasing, the ratio V_{eff}/Q_S is directly connected with the Purcell factor, and it defines the emission efficiency[27,28]. Indeed, to initiate photoluminescence for optical photoexcitation, strong interband transitions result in high absorption at the pump wavelength suppressing optical modes in the resonator, which allows to neglect resonant effects assuming $Q_P \sim 1$. In the SRS process, the resonant interaction at the pump wavelength becomes crucial and, as a result, the amplification depends on the term $V_{\mathrm{eff}}/Q_S Q_P$, according to Eq. (3). Thus, to improve the coupling efficiency and minimize the threshold for the nonlinear Raman amplification in a resonator, the optimization of two resonances is required.

Optimization of resonator parameters. For the Si nanoparticles with a fixed height (600 nm) placed on a sapphire substrate (Al_2O_3), the Q factor of the Mie-type modes can be calculated numerically [see Fig. 4(a)] in order to define the best parameters for experiment. The numerical study is performed with COMSOL software (for more details, see *Methods*). According to Eq. (3), the optimal SRS conditions correspond to the case when the pump wavelength λ_P=633 nm and Stokes wavelength λ_S=654 nm match the eigenmodes of the

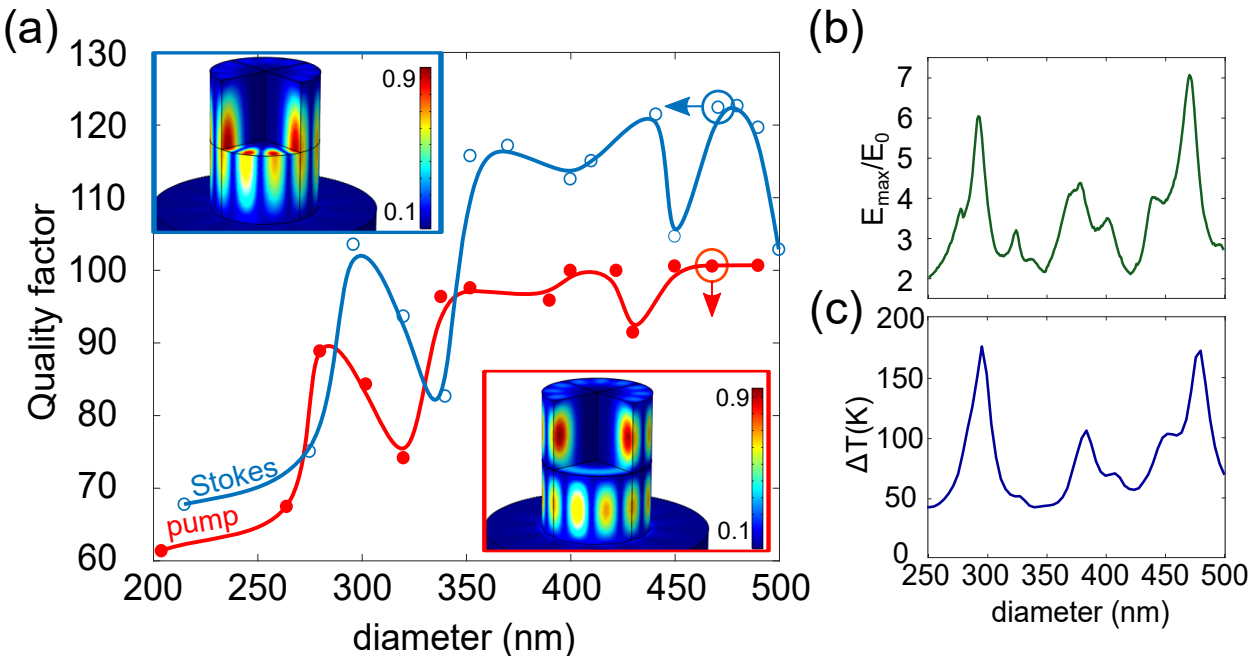

Figure 4: **Numerical study of resonant properties of nanoparticles.** (a) Quality factor of the eigenmodes of Si disks with 600 nm height for the wavelength 633 nm corresponding to the pump wavelength of the HeNe laser (filled red circles) and for the Raman Stokes emission wavelength (hollow blue circles). Insets show the normalized electric field magnitude distribution of the eigenmodes for the nanoparticle supporting stimulated Raman emission at pump and Stokes wavelengths. Color-bar scales are of normalized units. Solid lines are built for the ease of perception. (b) Numerical calculation of the field enhancement inside a single nanoparticle excited by a plane wave at 633 nm for varying diameters. (c) Numerical calculation of optical heating of a single nanoparticle with varying diameters.

nanoparticle. Figure 4(a) shows that this requirement can be fulfilled for a number of diameters. Remarkably, the values of the Q factor are generally higher for the Stokes wavelength because of lower material losses of c-Si in this spectral range as compared with the pump wavelength.

Although some of the eigenmodes have larger Q factors, they are difficult to be excited due to the symmetry constrains. The field distribution for an eigenmode is shown in Fig. 4(a), revealing its complex character. Figure 4(b) shows the local field enhancement for the excitation by a linear polarized plane wave, providing the important information that a plane wave with the linear polarization can excite efficiently the nanoparticle with diameter D=475 nm where both the maximum field enhancement (corresponding to calculated

coupling efficiency $B = 2.41$, see Section S5 of Supporting Information) and high Q factors ($Q_P \approx$100 and $Q_S \approx$120) can be achieved. Experimental measurements of the Raman intensity confirms that the Raman scattering signal takes a maximum value at D=475 nm, see Fig. 3(a). Finally, a spatial overlapping between pump and Stokes modes is an important parameter which affects the efficiency of SRS, according to Eq. (3). Our numerical calculations give the value $\Gamma \approx 0.784$ (see Section S5 of Supporting Information).

This analysis allows estimating a threshold for Raman lasing from Eq. (3) to understand better the observed phenomena. Namely, we use the Raman gain coefficient of c-Si as 76 cm/GW from Ref. 18 and parameters: λ_P=633 nm, λ_S=654 nm, $n_S \approx n_P \approx 3.8$ from Ref. 29, and $\mathrm{V_{eff}} = 0.108V$, where V is the nanoparticle volume (for details of numerical calculations, see Section S5 of Supporting Information). For the threshold, we obtain $P_{\mathrm{th}}^{\mathrm{calc}} \approx$ 250 mW, being two orders of magnitude higher than the experimental value $P_{\mathrm{exp}}^{\mathrm{tr}} = I_{\mathrm{P}}^{\mathrm{tr}} \cdot \pi r^2 \approx$ 3 mW. Along with the absence of spectral narrowing of the Raman peak[30], this means that we do not achieve the lasing threshold but instead demonstrate nonlinear amplification of the Raman scattering via stimulated emission mechanism.

Reduction of thermal overheating. Finally, we discuss the Mie-empowered thermal effects because c-Si has non-vanishing optical losses ($\alpha \approx 3.9\times10^4 \mathrm{cm}^{-1}$ from Ref. 29) at the pump wavelength λ_P=633 nm. As shown earlier[8,9,22], strong heating of Si nanoparticles can be achieved at critical coupling and low thermal conductivity of the substrate. For example, a spherical Si nanoparticle placed on a glass substrate can be heated up to 600 K under the conditions similar to our study[8]. Such a strong overheating reduces and broadens the Raman peak. In our design, we employ sapphire as the substrate material with much higher thermal conductivity ($\sim$40 $\mathrm{Wm^{-1}K^{-1}}$) as compared to silica glass ($\sim$1 $\mathrm{Wm^{-1}K^{-1}}$). Moreover, a tight contact of the nanoparticle with the substrate is better for a thermal sink than that for spherical nanoparticles[8,9] or nanowires[22]. Figure 4(c) shows the calculated average temperature of the nanoparticles with height 600 nm and different diameters. Despite the heating maximum is achieved also at $D = 475$ nm, it shows a weaker effect on optical proper-

ties of c-Si nanoparticles. However, this estimate suggests that the intensity of 1.1 MW/cm^2 is close to the limiting value due to overheating.

In summary, we have reported on the first observation of the stimulated Raman scattering from subwavelength crystalline silicon nanoparticles enhanced by Mie-type resonances. We have revealed the importance of critical optimization of the Q factors of nanoparticles, and thermal conductivity of a substrate to achieve a strong optical response and avoid overheating at higher intensities. We believe that our finding will be useful for advanced applications of resonant dielectric nanophotonics for nanoscale thermometry and biosensing, and we envision further studies of the stimulated Raman scattering in various nanophotonic designs[31–33].

Methods

Fabrication of samples. A set of single-crystal silicon nanoparticles (nanopillars and nanodisks) with different diameters placed on sapphire (Al_2O_3) substrates are fabricated by using a top-down technique. An epitaxial structure is grown by molecular beam epitaxy at 600° C using the Stranski-Krastanov growth mode. A set of isolated nanoparticle resonators with diameters variable with a 10-nm step in diameters is created on the grown epitaxial structure by applying focused gallium ion beam (FIB) milling using a FEI Versa 3D dual beam system. Ion current adjustment down to 1.5 pA allows to obtain nearly vertical side walls of the nanoparticles.

Optical characterisation. The experimental optical elastic scattering properties of the nanoparticles were studied by means of dark-field optical scattering technique. The setup consists of an infinity corrected objective (10×, NA = 0.26, Mitutoyo Plan Apo NIR) that is used for illumination with a white light source (HL-2000 halogen lamp) of the sample under angle 67^o to the substrate normal. The second objective (50×, NA = 0.42 Mitutoyo Plan Apo NIR) placed perpendicularly on top of the sample substrate is applied for acquiring the scattering signal. The scattered signal is analyzed by a confocal system with a spectrometer

(HORIBA LabRam HR) and cooled charge-coupled device (CCD) Camera (Andor DU 420A-OE 325) equipped with a 150 g/mm diffraction grating. The position of the nanoparticles is controlled by an additional CCD camera.

Raman scattering measurements. The experimental studies of Raman scattering experimental are performed with the confocal spectrometer (HORIBA LabRam HR) and confocal setup with 1800 g/mm diffractional grating allowing higher spectral resolution. The excitation source of 632.8 nm HeNe continuous wave laser focused through the optical microscope lens (100×, NA = 0.9 Mitutoyo Plan Apo HR) perpendicular to the sample substrate. The same objective is used for both excitation and collection of the Raman scattering signal. The employed laser system provides desired stability both in output intensity and laser spectral bandwidth of less than 0.002 nm (0.05 cm^{-1}), allowing precise Raman scattering measurements. The reflected signal is subsequently passed through 632.8 nm notch-filter in order to get rid of elastic scattering from the nanoparticles samples. A set of optical filters is used for varying the incident laser intensity on the nanoparticle samples.

Numerical simulations. For numerical simulations of the dark-field scattering, we employ the cylindrical symmetry of the problem to reduce it from fully three-dimensional to a two-dimensional electromagnetic problem. In the experimental setup, the incident TM-polarized plane wave (in-plane E-vector) excites the nanoparticle propagating at the angle of 67 degrees to normal. This plane wave is expanded into a series of the azimuthal harmonics $\sim e^{im\varphi}$ to calculate their contribution to the total scattering cross-section. We estimate the number of harmonics that have significant contributions to the total scattering by comparing the partial cross-sections with the results of the lower orders to include a finite number of them into the calculation. The commercial software COMSOL Multiphysics is used to model the computational domain size around 6 times larger than the size of a nanoparticle (this parameter is estimated from the computed dependence of the solution convergence from the size of the outer area). Physical domains include the cylindrical silicon nanoparticle (a rectangle in the plane projection), a sapphire substrate, and air. To avoid reflections from the

outer boundaries, the computational domain is surrounded by a PML-layer. The scattered radiation is collected in a solid angle with the angular opening of 49 degrees. Then, in the top of the model the line segment is selected where we calculate the radiation flow.

In the eigenmode calculations, we employ a three-dimensional model being important not only for the evaluation of the Q factor of the eigenmodes but also for the estimation of the field distribution inside the nanoparticle and the type of its symmetry. We employ the commercial numerical software COMSOL to study a cylindrical particle, its substrate, and the air surrounded by the cylindrical PML-layer. The size of the computational domain depends on the nanoparticle diameter, and it is approximately of 5-6 diameters. The study of the eigenmodes is conducted using the eigenfrequency module around the frequency corresponding to the incident wavelength. Analyzing the shift of the field distribution with the growth of the nanoparticle diameter, it is possible to estimate the configurations for which the eigenmode wavelength coincides with the initial one and select the nanoparticle with the best Q factors.

Optical heating. Calculations of optical heating are conducted by using numerical commercial software COMSOL Multiphysics. Fully three-dimensional problem for the electromagnetic wave propagation and heat transfer in solids is solved by using multi-physics solution. Computational domain consists of an outer sphere (radius 2 μm) placed on a sapphire hemisphere. Further computational steps are the same as described in Ref. 8.

Multipolar mode decomposition. The multipole mode decomposition of the radiation is performed by applying the approach described in Refs. 34,35. The basic multipole moments are evaluated by integrating numerically the total electric field inside the nanoparticle induced by a normally incident plane wave. Scattering power is decomposed up to the octupole terms, and higher-order terms are neglected. Further details can be found in Supporting Information.

Acknowledgements

This work was supported by the Ministry of Education and Science of the Russian Federation (Project 14.Y26.31.0010), the Grant of President of Russian Federation (MK-3514.2019.2), the Australian Research Council (grant DP200101168), and the Strategic Fund of the Australian National University. The authors are indebted to Filipp Komissarenko for the SEM images of nanoparticles, as well as Andrey Bogdanov and Kirill Koshelev for a help with numerical calculations. They also thank Anton Samusev, Dmitry Zuev, and Pavel Belov for fruitful discussions.

Associated content

Supporting Information is available free of charge at http://pubs.acs.org

Samples description. Details of multipole mode decomposition for silicon nanoparticles with and without a substrate. Description of the setups for dark-field and Raman scattering measurements. Details of connection between Raman spectral shift and local temperature of the nanoparticles. Raman scattering spectra for nanoparticles with diameters 300 nm and 350 nm. Calculations of optical properties (effective mode volume, coupling efficiency, modes overlapping, and field-components) for the nanoparticle with diameter 475 nm at pump and Stokes wavelengths.

References

1. Kneipp, K.; Moskovits, M.; Kneipp, H. *Surface-enhanced Raman scattering: physics and applications*; Springer Science & Business Media, 2006; Vol. 103.

2. Ding, S.-Y.; Yi, J.; Li, J.-F.; Ren, B.; Wu, D.-Y.; Panneerselvam, R.; Tian, Z.-Q. Nanostructure-based plasmon-enhanced Raman spectroscopy for surface analysis of materials. *Nature Reviews Materials* **2016**, *1*, 1–16.

3. Rodriguez, I.; Shi, L.; Lu, X.; Korgel, B. A.; Alvarez-Puebla, R.; Meseguer, F. Silicon nanoparticles as Raman scattering enhancers. *Nanoscale* **2014**, *6*, 5666–5670.

4. Caldarola, M.; Albella, P.; Cortés, E.; Rahmani, M.; Roschuk, T.; Grinblat, G.; Oulton, R. F.; Bragas, A. V.; Maier, S. A. Non-plasmonic nanoantennas for surface enhanced spectroscopies with ultra-low heat conversion. *Nature Communications* **2015**, *6*, 1–8.

5. Alessandri, I.; Lombardi, J. R. Enhanced Raman scattering with dielectrics. *Chemical Reviews* **2016**, *116*, 14921–14981.

6. Dmitriev, P. A.; Baranov, D. G.; Milichko, V. A.; Makarov, S. V.; Mukhin, I. S.; Samusev, A. K.; Krasnok, A. E.; Belov, P. A.; Kivshar, Y. S. Resonant Raman scattering from silicon nanoparticles enhanced by magnetic response. *Nanoscale* **2016**, *8*, 9721–9726.

7. Frizyuk, K.; Hasan, M.; Krasnok, A.; Alú, A.; Petrov, M. Enhancement of Raman scattering in dielectric nanostructures with electric and magnetic Mie resonances. *Physical Review B* **2018**, *97*, 085414.

8. Zograf, G. P.; Petrov, M. I.; Zuev, D. A.; Dmitriev, P. A.; Milichko, V. A.; Makarov, S. V.; Belov, P. A. Resonant non-plasmonic nanoparticles for efficient temperature-feedback optical heating. *Nano Letters* **2017**, *17*, 2945–2952.

9. Milichko, V. A.; Zuev, D. A.; Baranov, D. G.; Zograf, G. P.; Volodina, K.; Krasilin, A. A.; Mukhin, I. S.; Dmitriev, P. A.; Vinogradov, V. V.; Makarov, S. V.; Belov, P. A. Metal-dielectric nanocavity for real-time tracing molecular events with temperature feedback. *Laser & Photonics Reviews* **2018**, *12*, 1700227.

10. Zograf, G. P.; Timin, A. S.; Muslimov, A. R.; Shishkin, I. I.; Nominé, A.; Ghanbaja, J.; Ghosh, P.; Li, Q.; Zyuzin, M. V.; Makarov, S. V. All-optical nanoscale heating and thermometry with resonant dielectric nanoparticles for controllable drug release in living cells. *Laser & Photonics Reviews* **2020**, 1900082.

11. Rutckaia, V.; Heyroth, F.; Novikov, A.; Shaleev, M.; Petrov, M.; Schilling, J. Quantum dot emission driven by Mie resonances in silicon nanostructures. *Nano Letters* **2017**, *17*, 6886–6892.

12. Zhang, C.; Xu, Y.; Liu, J.; Li, J.; Xiang, J.; Li, H.; Li, J.; Dai, Q.; Lan, S.; Miroshnichenko, A. E. Lighting up silicon nanoparticles with Mie resonances. *Nature Communications* **2018**, *9*, 1–7.

13. Tiguntseva, E.; Zograf, G.; Komissarenko, F.; Zuev, D.; Zakhidov, A.; Makarov, S.; Kivshar, Y. S. Light-emitting halide perovskite nanoantennas. *Nano Letters* **2018**, *18*, 1185–1190.

14. Prince, R. C.; Frontiera, R. R.; Potma, E. O. Stimulated Raman scattering: from bulk to nano. *Chemical Reviews* **2017**, *117*, 5070–5094.

15. Qian, S.-X.; Chang, R. K. Multiorder Stokes emission from micrometer-size droplets. *Physical Review Letters* **1986**, *56*, 926.

16. Lin, H.-B.; Huston, A.; Eversole, J. D.; Campillo, A. J. Double-resonance stimulated Raman scattering in micrometer-sized droplets. *Journal of the Optical Society of America B* **1990**, *7*, 2079–2089.

17. Spillane, S.; Kippenberg, T.; Vahala, K. Ultralow-threshold Raman laser using a spherical dielectric microcavity. *Nature* **2002**, *415*, 621–623.

18. Claps, R.; Dimitropoulos, D.; Han, Y.; Jalali, B. Observation of Raman emission in silicon waveguides at 1.54 μm. *Optics Express* **2002**, *10*, 1305–1313.

19. Claps, R.; Dimitropoulos, D.; Raghunathan, V.; Han, Y.; Jalali, B. Observation of stimulated Raman amplification in silicon waveguides. *Optics Express* **2003**, *11*, 1731–1739.

20. Yang, X.; Wong, C. W. Design of photonic band gap nanocavities for stimulated Raman amplification and lasing in monolithic silicon. *Optics Express* **2005**, *13*, 4723–4730.

21. Wu, J.; Gupta, A. K.; Gutierrez, H. R.; Eklund, P. C. Cavity-enhanced stimulated Raman scattering from short GaP nanowires. *Nano Letters* **2009**, *9*, 3252–3257.

22. Agarwal, D.; Ren, M.-L.; Berger, J. S.; Yoo, J.; Pan, A.; Agarwal, R. Nanocavity-enhanced giant stimulated Raman scattering in Si nanowires in the visible light region. *Nano Letters* **2019**, *19*, 1204–1209.

23. Baryshnikova, K. V.; Frizyuk, K.; Zograf, G.; Makarov, S.; Baranov, M. A.; Zuev, D.; Milichko, V. A.; Mukhin, I.; Petrov, M.; Evlyukhin, A. Revealing low-radiative modes of nanoresonators with internal Raman scattering. *JETP Letters* **2019**, *110*, 25–30.

24. Hon, N. K.; Soref, R.; Jalali, B. The third-order nonlinear optical coefficients of Si, Ge, and Si_{1-x} Ge_x in the mid-wave and long-wave infrared. *Journal of Applied Physics* **2011**, *110*, 9.

25. Hopkins, R. J.; Symes, R.; Sayer, R. M.; Reid, J. P. Determination of the size and composition of multicomponent ethanol/water droplets by cavity-enhanced Raman scattering. *Chemical Physics Letters* **2003**, *380*, 665–672.

26. Grudinin, I. S.; Maleki, L. Ultralow-threshold Raman lasing with CaF2 resonators. *Optics Letters* **2007**, *32*, 166–168.

27. Suhr, T.; Gregersen, N.; Yvind, K.; Mørk, J. Modulation response of nanoLEDs and nanolasers exploiting Purcell enhanced spontaneous emission. *Optics Express* **2010**, *18*, 11230–11241.

28. Khurgin, J. B.; Sun, G. Comparative analysis of spasers, vertical-cavity surface-emitting lasers and surface-plasmon-emitting diodes. *Nature Photonics* **2014**, *8*, 468.

29. Aspnes, D. E.; Studna, A. Dielectric functions and optical parameters of Si, Ge, GaP, GaAs, GaSb, InP, InAs, and InSb from 1.5 to 6.0 ev. *Physical Review B* **1983**, *27*, 985.

30. Rong, H.; Liu, A.; Jones, R.; Cohen, O.; Hak, D.; Nicolaescu, R.; Fang, A.; Paniccia, M. An all-silicon Raman laser. *Nature* **2005**, *433*, 292–294.

31. Ha, S. T.; Fu, Y. H.; Emani, N. K.; Pan, Z.; Bakker, R. M.; Paniagua-Domínguez, R.; Kuznetsov, A. I. Directional lasing in resonant semiconductor nanoantenna arrays. *Nature Nanotechnology* **2018**, *13*, 1042–1047.

32. Koshelev, K.; Kruk, S.; Melik-Gaykazyan, E.; Choi, J.-H.; Bogdanov, A.; Park, H.-G.; Kivshar, Y. Subwavelength dielectric resonators for nonlinear nanophotonics. *Science* **2020**, *367*, 288–292.

33. Tiguntseva, E.; Koshelev, K.; Furasova, A.; Tonkaev, P.; Mikhailovskii, V.; Ushakova, E. V.; Baranov, D. G.; Shegai, T.; Zakhidov, A. A.; Kivshar, Y.; Makarov, S. Room-Temperature Lasing from Mie-Resonant Non-Plasmonic Nanoparticles. *ACS Nano, doi.org/10.1021/acsnano.0c01468*.

34. Alaee, R.; Rockstuhl, C.; Fernandez-Corbaton, I. An electromagnetic multipole expansion beyond the long-wavelength approximation. *Optics Communications* **2018**, *407*, 17–21.

35. Evlyukhin, A. B.; Chichkov, B. N. Multipole decompositions for directional light scattering. *Physical Review B* **2019**, *100*, 125415.

Graphical TOC Entry